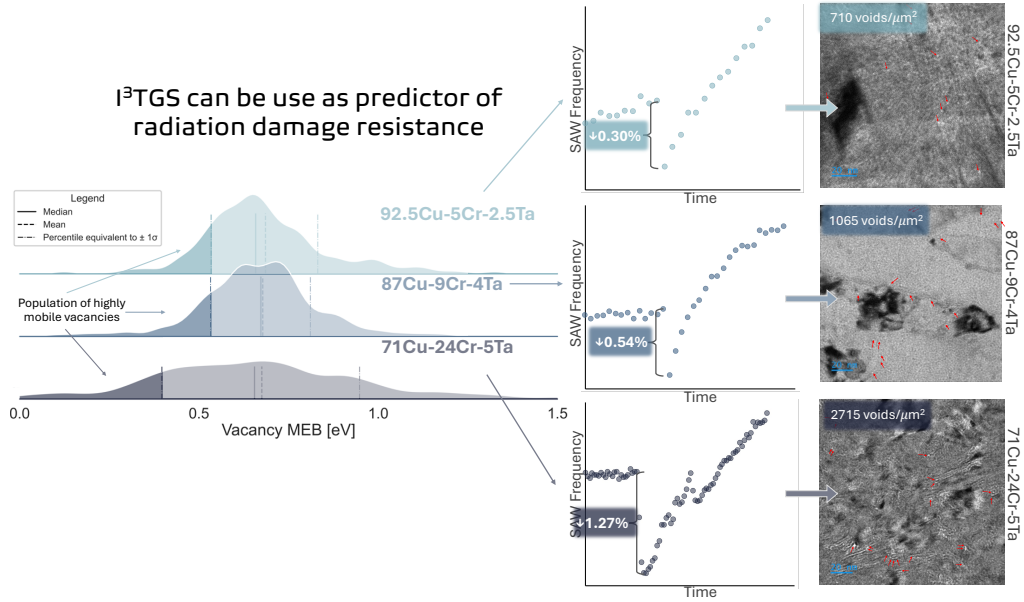


Graphical Abstract

Rapid Primary Radiation Damage Resistance Assessment of Precipitation-Hardened Cu Alloys

Elena Botica-Artalejo, Gregory Wallace, Michael Short



Highlights

Rapid Primary Radiation Damage Resistance Assessment of Precipitation-Hardened Cu Alloys

Elena Botica-Artalejo, Gregory Wallace, Michael Short

- In situ transient grating spectroscopy reveals an immediate SAW frequency response to irradiation that is able to provide relative comparison of final void accumulation between different samples.
- Vacancy MEB distributions explain the susceptibility to form voids, by the population of mobile vacancies.
- This methodology enable rapid screening of radiation damage resistance materials, reducing irradiation and characterization times.

Rapid Primary Radiation Damage Resistance Assessment of Precipitation-Hardened Cu Alloys

Elena Botica-Artalejo^{a,b}, Gregory Wallace^a, Michael Short^{a,c}

^a*Plasma Science and Fusion Center (PSFC), Cambridge, 02139, MA, USA*

^b*Department of Materials Science & Engineering, Cambridge, 02139, MA, USA*

^c*Department of Nuclear Science & Engineering, Cambridge, 02139, MA, USA*

Abstract

This study establishes a direct correlation between in situ irradiation-induced property changes measured by transient grating spectroscopy (TGS) and the resulting microstructural damage in Cu–Cr–Ta alloys. Thin films fabricated by physical vapor deposition were irradiated with 6.6 MeV Cu^{+3} ions up to 25 DPA, while TGS continuously monitored the evolution of surface acoustic wave (SAW) frequency and thermal diffusivity. Post-irradiation transmission electron microscopy (TEM) was used to quantify void formation as a metric of accumulated radiation damage. A pronounced decrease in SAW frequency was observed some seconds after the onset of irradiation, and it was found to correlate strongly with the final void density. Vacancy MEB calculations propose that the small decrease in SAW frequency is associated with the low population of mobile vacancies, promoting defect recombination and decreasing void formation. This relationship enables early prediction of relative radiation damage resistance within minutes of irradiation, substantially reducing the time required compared to conventional irradiation and post-characterization routes, allowing rapid screening of multiple compositions. We were able to test this method with 3 compositions of the Cu–Cr–Ta system. More generally, this in situ approach provides an efficient pathway for accelerating the development of materials for radiation environments.

Keywords: *In situ* Irradiation, TGS, Nuclear materials, Cu-alloys, GRCop-84

1. Introduction

Fusion technology presents exceptional challenges across multiple scientific disciplines, particularly in materials science, where it imposes extreme demands on structural and functional components. All plasma-facing components (PFCs) are subject to intense fluxes of neutrons, ions, and thermal energy. To perform reliably in this environment, PFCs must meet a stringent set of common requirements, including low activation, minimal sputtering erosion, low tritium retention, a high melting point, and stable thermo-mechanical properties. Beyond these baseline criteria, specialized applications introduce further constraints. A prominent example is the radio-frequency (RF) antenna, used to heat plasma to ignition temperatures in tokamaks, which must satisfy additional performance specifications. These RF antennas must exhibit high electrical conductivity to mitigate resistive losses and demonstrate low susceptibility to arcing under high-power conditions [1]. As these components are designed for continuous, maintenance-free operation over extended durations—spanning months or years—their ability to withstand the fusion environment without degradation is paramount.

The development of viable lower hybrid current drive (LHCD) launchers is critically constrained by the lack of a material that satisfies all operational, thermal-mechanical, and radiological requirements simultaneously [2]. A leading candidate is the precipitation-hardened copper alloy GRCop-84 (Cu-8Cr-4Nb, at.%), which excels in several key performance areas, and has been used for construction of the LHCD [3] and reflectometer [4] antennas in the DIII-D tokamak. Its strength derives from a dispersion of fine, thermally stable Cr_2Nb (C15 Laves phase) precipitates within the $\mu\text{m} - \text{nm}$ size range, which resist coarsening up to 800°C and pin Cu grain boundaries, maintaining microstructural integrity [5, 6]. Consequently, GRCop-84 exhibits high strength, low creep, and excellent thermal and electrical properties—with thermal diffusivity and electrical resistivity ($\sim 8.310^{-5}\text{m}^2/\text{s}$ and $\sim 3\mu\Omega \cdot \text{cm}$ at 100°C , respectively) comparable to oxygen-free copper [7, 8, 9]. These attributes make it an exceptional candidate for RF components [10, 11].

However, its viability for fusion is ultimately limited by the 4 at.% niobium content, which presents a severe radiological drawback. For a material to qualify as low-level waste (LLW), a prerequisite for the social license of fusion power [12], it must achieve a waste disposal rating (WDR) below 1. The WDR is the sum of the ratios between an element's concentration

divided by that element’s maximum allowable concentration after irradiation, considering its potential to become dangerously radioactive. The Nb in GRCop-84 leads to a calculated WDR of ~ 2400 after 1.7 years of operation [13], orders of magnitude above the acceptable threshold and far exceeding the established limit of 0.4–9 ppm for Nb in first-wall materials [14].

This fundamental discrepancy creates a clear imperative: to develop Nb-free copper alloys that retain the beneficial C15 Laves phase precipitate strengthening while achieving a low WDR. The key to this new material system lies in replicating or replacing the stabilizing Cr_2Nb intermetallics. Fabrication of such microstructures typically requires rapid solidification techniques, such as laser power bed fusion (LPBF) of gas atomized GRCop-84 powder, or even vapor deposition techniques such as physical vapor deposition (PVD) or chemical vapor deposition (CVD), to achieve the necessary fine-scale precipitates while avoiding detrimental grain growth or uneven distribution of the precipitates.

Recent efforts to develop alloys with reduced niobium content have achieved some success. For instance, Perrin et al. [15] investigated the Cu-Cr-Nb-Zr system to enhance the strength and creep life of ITER’s baseline Cu-Cr-Zr alloy, demonstrating that Laves phase precipitates improve mechanical properties without degrading thermal and electrical conductivity post-irradiation. Nevertheless, the Nb content remains a limiting factor. Other candidate systems, such as Cu-Ni-Be [16] and Cu- Al_2O_3 [17], are constrained by their maximum operating temperatures. Among elements capable of forming C15 Laves phases with chromium, tantalum (Ta) emerges as a particularly promising alternative [18]. Supporting this, Li et al. [19] recently demonstrated that a Cu-rich Cu-Cr-Ta alloy offers high-temperature mechanical property enhancements respect Cu-Cr, taking advantage of the Laves phase precipitates, establishing this system as a compelling candidate for further investigation.

The present study examines the Cu-Cr-Ta alloy system as a prospective Nb-free material for RF antenna applications in fusion environments. To evaluate primary radiation damage resistance, a series of compositions were subjected to in situ heavy-ion irradiation. During irradiation, the materials’ elastic properties were monitored in real time via transient grating spectroscopy (TGS), tracking the values of the surface acoustic wave frequency. This approach provides a high-throughput screening method, using the correlation of the immediate SAW frequency shift observed at beam onset with the material’s propensity for vacancy creation, offering a rapid indicator of radiation tolerance. Findings from this in situ analysis were directly corrobo-

rated by post-irradiation examination using transmission electron microscopy (TEM), and the vacancy migration energy barrier (MEB) distributions from each system supported the findings.

2. Methods

2.1. High-throughput material generation

The material of study from this work has been thick films ($\sim 4 - 5\mu m$) of combinatorial physically vapor deposited Cu alloys, changing its composition in a planar configuration along several 1-inch Si wafers, as depicted in Figure 1. Cu-Cr-Ta combinatorial thick films were deposited using physical vapor deposition in a Kurt J. Lesker PVD 75 PRO Line, enabling 2D gradient compositional films by independently controlling three sputtering targets favoring Cu-rich films (deposition parameters can be seen in Table 1). To ensure a homogeneous deposition conditions between different elements, the three sputtering targets were arranged symmetrically at 120° separations, with each gun fixed at an identical inclination toward the substrate to create different concentrations patterns. The power for each target was adjusted to vary the amount relative concentration of each element. The following high-purity Kurt J. Lesker targets were employed: Cu (99.99%), Cr (99.95%) and Ta (99.95%). Impurity certifications are available in the associated data repository. Prior to deposition, a Ti (99.995% pure) adhesion layer was applied to enhance substrate bonding and act as an oxygen getter, reducing contamination. The films were grown on 1-inch p-type (B-doped) semi-prime quality silicon wafers with $R_a < 0.5\mu m$. A total of 21 wafers are obtained per deposition, with a variation between 0.5-2 at.% depending on the element considered.

2.2. Microscopy characterization

The elemental composition on each wafer was obtained by energy-dispersive X-ray spectroscopy (EDS) using a Zeiss Gemini 450 scanning electron microscope (SEM). The gun energy was set to 25kV, to excite the characteristic X-ray lines and sampling a reasonable depth of the material. The working distance was maintained at 8.5 nm for optimal X-ray detection efficiency. In EDS analysis, carbon and oxygen spectral peaks were deconvolved to determine relative elemental concentrations while accounting for potential surface contaminants. A summary of sample compositions and the tests performed on each is provided in Table 2.

Table 1: Deposition parameters for Cu-Cr-Ta thick films.

Parameter	Value
Vacuum level prior to deposition (Torr)	7.4×10^{-6}
Chamber pressure at deposition (Torr)	6.2×10^{-4}
Sputtering time (min)	150
Gas flow (sccm)	20
Gas species	Argon (99.999%)
Temperature ($^{\circ}\text{C}$)	20–25
Cu target power & size (Watts/inch/type)	150/2/DC
Cr target power & size (Watts/inch/type)	80/2/RF
Ta target power & size (Watts/inch/type)	30/2/DC
Ti target power & size (Watts/inch/type)	60/2/DC
Ti sputtering time (min)	60

Table 2: Chemical composition and corresponding batch for Cu-Cr-Ta thick films.

SampleID	Cu (at.%)	Cr (at.%)	Ta (at.%)
044_04	92.6	4.9	2.5
044_15	86.9	9.2	3.8
044_18	70.4	24.3	5.3

Transmission electron microscopy (TEM) was utilized to characterize the damage induced by the ion beam. Void structures were imaged in conventional TEM mode using a JEOL F200 microscope operating at an accelerating voltage of 200 kV. A $30\mu\text{m}$ objective aperture was employed to mitigate contrast from other microstructural features. Subsequent image analysis, performed with Fiji software, enabled the quantification of void density through manual counting and sizing, using the ROI Manager function under the Process menu of the software.

Complementary chemical analysis was conducted via energy-dispersive X-ray spectroscopy (EDS) on both irradiated and unirradiated regions to identify radiation-induced compositional and microstructural changes. Finally, electron energy loss spectroscopy (EELS) was performed in some of the TEM lamellas to know the thickness of them. The EDS and EELS analysis were done using the Thermo Fisher Scientific (TFS) Themis Z G3 aberration-corrected scanning transmission electron microscope (STEM) with a voltage of 300kV. To prepare the lamellas for TEM analysis the FEI Helios 660 focus

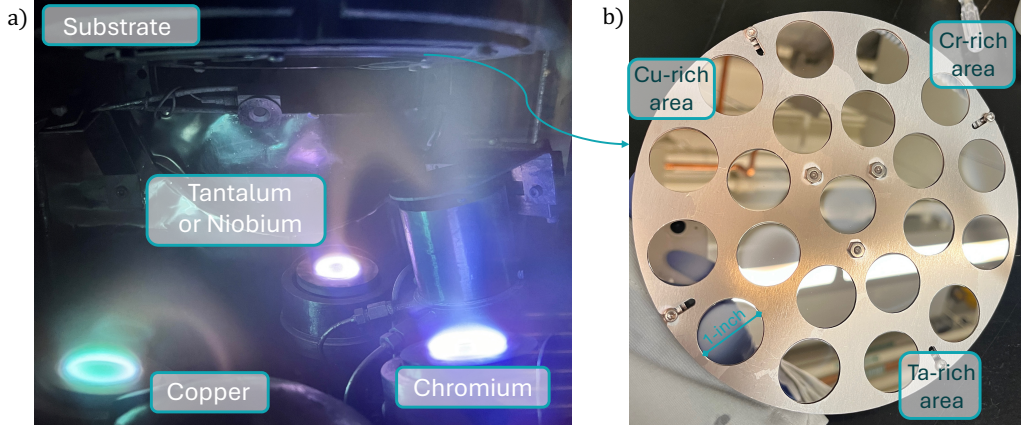


Figure 1: a) Combinatorial deposition of Cu-Cr-Ta alloys. b) Substrate holder with Si wafers after deposition.

ion beam (FIB) was used. Samples were progressively milled down up to $40 - 50\mu m$ by reducing the ion current from $30kV$ to $2kV$.

Prior to TEM inspection a surface cleaning was performed using a Fischione 1051 TEM mill to eliminate any Ga damage and surface oxides, which readily form on copper.

2.3. *In situ ion irradiation coupled with transient grating spectroscopy*

Transient grating spectroscopy (TGS) is a non-contact, laser-based method used to quantitatively measure a material's elastic properties and thermal diffusivity at controlled depths [20]. The technique provides localized measurements of the thermo-elastic response with a spatial resolution determined by the focal width of the probe laser. Figure 2 illustrates the conceptual setup when TGS is coupled with ion beam irradiation. A pump laser ($1kHz$, $532nm$, $\sim 500ps$ pulses) excites the material surface, generating a grating pattern with an on-sample power of $7.4mW$. The grating spacing determines the maximum depth for probing thermo-elastic properties. A continuous-wave probe laser ($577nm$) then monitors the surface excitation via first-order diffraction, with an intensity of approximately $127kWm^{-2}$. Table 3 details all relevant TGS parameters. The probe beam measures the surface acoustic wave (SAW) frequency, which relates to elastic properties, and the signal decay provides the thermal diffusivity. The total signal intensity, $(I_{tot}(t))$, is described by:

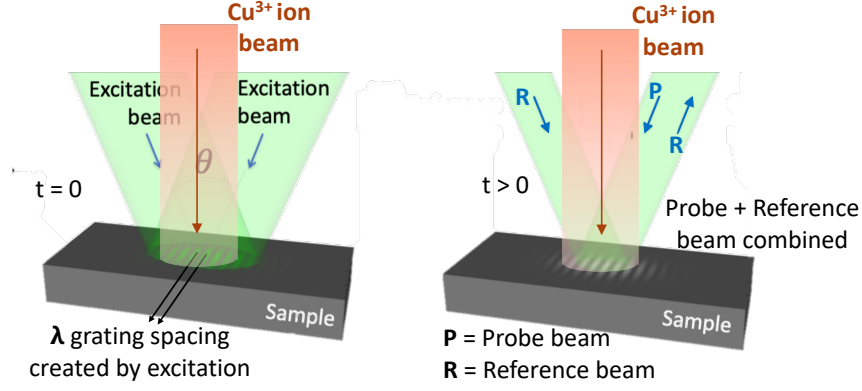


Figure 2: Schematic of TGS coupled with in situ ion irradiation. Adapted from [20].

$$I_{tot}(t) = A \left[\operatorname{erfc} \left(q_0 \sqrt{\alpha_x t} + \frac{\beta}{\sqrt{t}} e^{-q_0^2 \alpha_x t} \right) \right] + B \left[\sin(2\pi f_{SAW} t + \Theta) e^{-t/\tau} \right] + C \quad (1)$$

where $q_0 = 2\pi/\Lambda$ is the grating wavenumber originated from the $\Lambda[m]$ TGS grating space (in the present system configuration the focusing length is 1:1 through the phase mask, making Λ being indistinguishable from the wavelength λ), $\alpha_x[m^2 s^{-1}]$ is the in-plane thermal diffusivity, $\beta[s^{1/2}]$ represents the ratio of displacement-to-reflectivity contributions, $f_{SAW}[Hz]$ is the SAW frequency, Θ is the phase, and $\tau[s]$ is the decay time. Constants A , B , and C are determined through nonlinear fitting of experimental data [21].

The SAW frequency is related to elastic properties via the Rayleigh wave equation [22]:

$$c_r = f_{SAW} \lambda = \sqrt{\frac{E}{\rho}} \quad (2)$$

where $\lambda[m]$ is the spatial period of the surface grating, $E[Pa]$ is Young's modulus, and $\rho[kg/m^3]$ is the material density. For isotropic materials, this provides a quantitative measure, allowing the SAW frequency to be expressed as:

$$f_{SAW} = \frac{1}{\lambda} \sqrt{\frac{E}{\rho}} \quad (3)$$

For anisotropic materials, such as most polycrystals, absolute values are more appropriate, given the technique’s spot size relative to grain dimensions. In this case, as we deal with a nanocrystalline microstructure, it can be assumed that we are obtaining an average value from different grains, as the spot size area is 10^4 times greater than the average grain size of the samples presented on this work.

A 0.2% neutral density filter was employed to reduce the on-sample pump power to $5.89mW$. A di-homodyne phase collection geometry was used [23], employing two phase-locked probe beams ($\phi = \pm\frac{\pi}{2}$) to stabilize the signal against phase fluctuations. The current experimental setup is detailed in [21]. The probing depth can be adjusted by changing the grating spacing, Λ , with nominal sensitivities of λ/π for thermal properties [24] and $\lambda/2$ for SAW signals [22]. A spacing of $\lambda = 3.4\mu m$ was selected to match the ion-damaged region depth. Daily calibrations using a single-crystal tungsten 100 sample ensured accurate grating spacing values, accounting for minor variations ($< \pm 0.1\mu m$) due to ambient conditions.

Time resolution was optimized and settled on 2000 traces per 10 seconds, which improved temporal resolution without compromising data quality. A custom MATLAB code processed raw TGS data to extract SAW frequency and thermal diffusivity [25]. Both raw and processed data are available in this article’s data repository.

The TGS system was mounted pointing to a chamber viewport, enabling in situ monitoring during irradiation. Samples were rotated 45° relative to the ion beam to maintain perpendicular alignment with the TGS system, required for di-homodyne signal formation.

Irradiations were performed at the Cambridge Laboratory for Accelerator Surface Science (CLASS) at the MIT Plasma Science and Fusion Center, using tandem ion accelerator at 1.65 MV. Experiments employed Cu^{3+} ions at 6.6 MeV at around $250^\circ C$. Flux rates ranged from $5 \times 10^{16} ions/m^2 \cdot s$ to $6 \times 10^{16} ions/m^2 \cdot s$. Beam current was monitored with a picoammeter connected to the sample holder, isolated electrically from the rest of the beamline. A 2 mm aperture focused the beam, producing an ellipsoidal spot of $4.44 mm^2$ on the angled sample. Prior to experiments, beam alignment with the TGS spot was verified using a silver-activated zinc sulfide coating on a ceramic substrate of 1 mm thick laid on top of the sample.

Ion penetration depth and damage profiles were simulated using SRIM [26], following the procedure indicated in [27] with modified displacement energies of 30 eV for Cu, 40 eV for Cr and 90 eV for Ta, according to [28],

Parameter	Value
Pump wavelength	532 nm
Pump energy per pulse	10 μ J
Pump pulse duration	<500 ps
Pump spot size (on-sample diameter)	150 μ m
Pump firing frequency	1 kHz
Pump on-sample power	7.36 mW
Probe wavelength	671 nm
Probe frequency	Continuous Wave
Probe spot size (on-sample diameter)	90 μ m
Probe on-sample power	4.6 mW
Detector bandwidth	50 kHz - 1 GHz (3 dB)
Oscilloscope bandwidth	5 GHz
Averaged traces per second	2000
Calibrated on-sample grating spacing	3.4 μ m
Sample roughness	$R_a = 10 \text{ \AA}$

Table 3: Detailed summary of TGS system parameters. Spot sizes reported as 2σ Gaussian widths.

obtaining a penetration depth of $2\mu\text{m}$.

2.4. CALPHAD calculations

CALPHAD calculations were performed using the software Thermo-Calc 2024b with the TCHEA7 database for high entropy alloys. Thermal conductivity and electrical conductivity calculations were performed, ranging the composition from pure Cu to pure Cr_2X , replacing X with different elements that form C15 laves phases as Nb does [18], like Zr, Ta, and Hf.

2.5. Nudge Elastic Band calculations

Climbing-image nudged elastic band (CI-NEB) calculations were performed with VASP to determine the vacancy migration energy barrier (MEB) in three Cu-based alloy systems. A $2\times 2\times 2$ FCC supercell containing 64 atoms was employed. The supercells were generated using a Python script that randomly placed the constituent atoms according to the specified concentrations. Each system was initially relaxed to obtain a stable reference structure. Subsequently, another script was used to remove a Cu atom at the center of the

supercell, creating a vacancy. The resulting configuration was relaxed without allowing changes to the supercell volume. Additional relaxed structures were generated by moving the vacancy position to each of the 12 nearest-neighbor (NN) positions relative to the original site. For each system, 20 random systems were generated.

The CI-NEB calculations were then performed using the relaxed microstructure with the central vacancy as the initial state and the vacancy-relaxed NN configurations as the final states of the migration pathway. A total of five intermediate images were used to construct the MEB profile. To account for the MEB value of a system, the calculated energy to move forward and backward was taken into account, implying 480 values for taking the average of the MEB for each of the alloy systems.

Python scripts to create the supercell and NEB images, as well as, INCAR files for each calculation can be found in the Github repository of this manuscript.

3. Results

3.1. Thermal conductivity calculations for Cu-based alloy systems

A computational screening of candidate Cu–Cr–X systems was conducted using the CALPHAD method to assess thermal and electrical conductivity. The ternary element X was restricted to Zr, Ta, Nb, and Hf, all of which are known to form stabilizing C15 Laves phases with Cr [18], to obtain a precipitation-hardened alloy. To ensure a consistent comparison, the atomic composition was held equivalent to that of GRCo-84, with Nb replaced by each candidate.

The results, presented in Figure 3, indicate that the Ta-substituted alloy possesses the highest calculated thermal conductivity. Through the Wiedemann–Franz relation [29], this also implies superior electrical conductivity, projecting performance that may surpass the GRCo-84 benchmark.

3.2. TGS monitoring during self-ion irradiation

Thermo-elastic properties were monitored during self-ion irradiation in 3 different samples of the Cu–Cr–Ta system, using the **In situ Ion Irradiation** experiments in combination with **TGS** measurements (I^3TGS). These type of measurements not only give information related to the evolution of the thermo-elastic properties of the material, but also allow to infer the relative radiation damage in the sample and compare it to other alloys manufactured

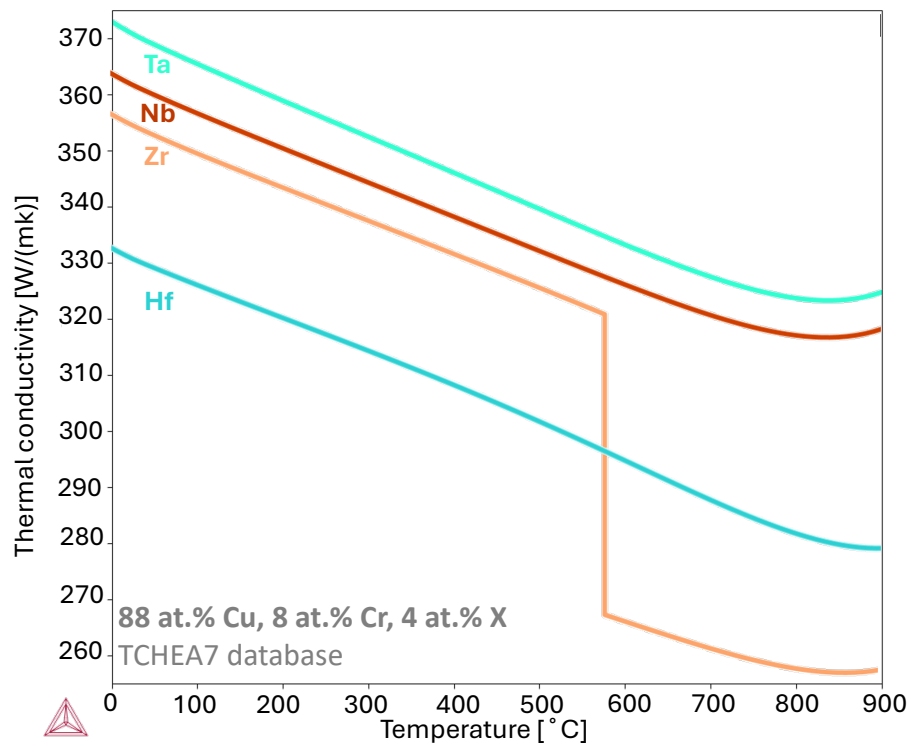


Figure 3: CALPHAD Thermal conductivity evaluation between different candidate elements in the 88 at.%Cu-8 at.%Cr-4at.%X system. TCHEA7 database was employed.

under the same conditions [30] by monitoring the fluctuation of the SAW frequency. During these experiments samples have been irradiated continuously up to 25 DPA using 6.5 MeV Cu^{3+} at 250°C to promote vacancy clustering [31] in order to facilitate void visualization, at the same time thick film integrity was guaranteed. When irradiation temperatures were close to 300°C , film delamination was observed during cool down, hence irradiation temperature was reduced to 250°C . Figure 4 shows the evolution of SAW frequency with time for a flux rate of $5.6 \times 10^{16} \text{ ions}/\text{m}^2 \cdot \text{s}$ when using a beam current of 120 nA . Additionally, it can be seen the evolution of temperature and current during the whole irradiation time. It is noticeable a initial drop in the SAW frequency upon beam start, around 0.1-0.2 DPA. At this dose, some authors have identified the point defect saturation level for copper alloys after monitoring properties like electrical resistivity, thermal resistivity or hardening [32, 33, 34, 35]. A similar profile, with the same trend was obtained for the other samples in the present work. It's noticeable that the sample that shows the smallest drop of the SAW frequency, around 0.07 DPA, is the Cu-5 at.% Cr-2.5 at.% Ta. The values of the SAW frequency drop for each alloy can be seen on table 4.

3.3. Radiation damage assessment through transmission electron microscopy

To quantify radiation damage, the void density was determined from TEM images. All samples were examined in conventional TEM (CTEM) mode using the overfocus-underfocus technique [36], with defocus values of $\pm 1 \mu\text{m}$ relative to the focused condition (see Figure 5). Figure 6 summarizes the void size and number distributions for each sample, together with the corresponding void densities. The highest void density is observed in the Cu-24 at.% Cr-5 at.% Ta alloy, followed by Cu-9 at.% Cr-4 at.% Ta, while Cu-5 at.% Cr-2.5 at.% Ta exhibits the lowest void density. A consistent trend is also observed in the SAW frequency drop, which increases with increasing void density. A direct comparison of the void density and SAW frequency drop trends is provided in Table 4. To assess the effects of irradiation on the remaining microstructure, EDS was performed on both irradiated and unirradiated samples. Figure 7 compares unirradiated (Fig. 7a) and irradiated (Fig. 7b) lamella extracted parallel to the irradiation direction from the Cu-5 at.% Cr-2.5 at.% Ta alloy. The unirradiated microstructure exhibits a homogeneous distribution of thin elongated Cr_2Ta precipitates. In contrast, the irradiated lamella shows a marked reduction of these precipitates within the damage region, with precipitates predominantly observed

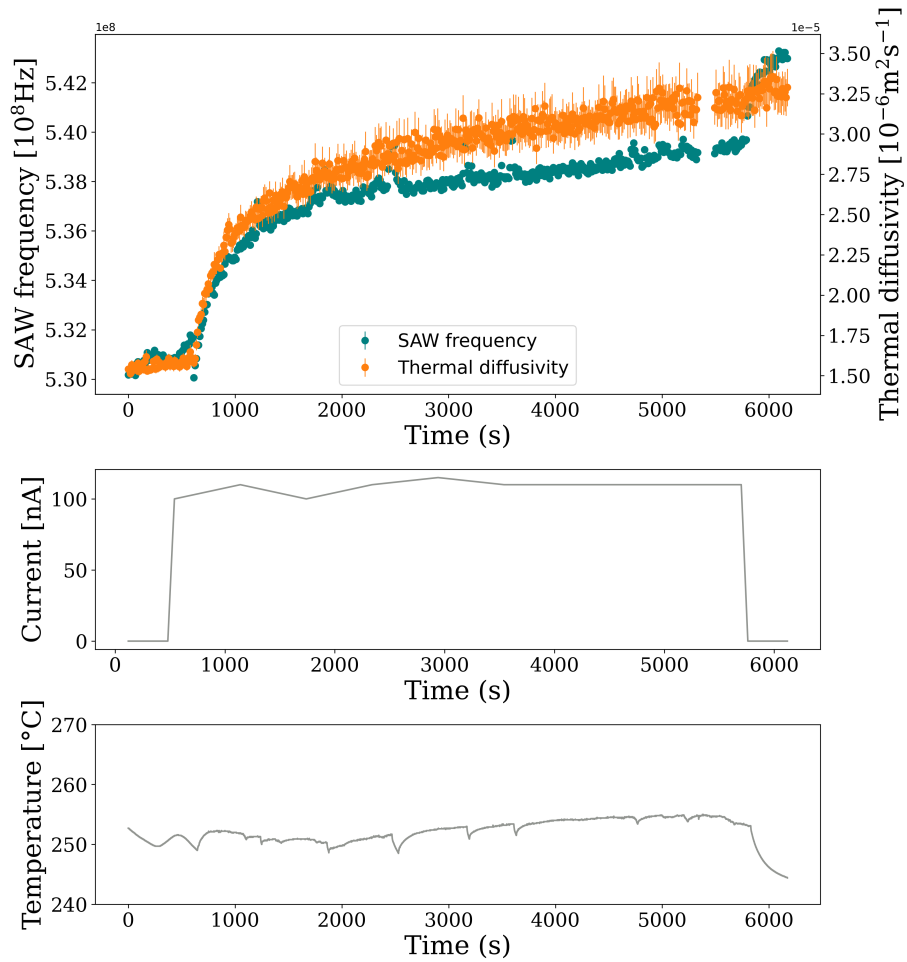


Figure 4: I^3TGS results from the Cu-5 at.% Cr-2.5 at.% Ta sample irradiated at 6.5 MeV with Cu^{3+} ions at 250°C . Blue dots correspond to SAW frequency values and orange dots to thermal diffusivity.

beyond the penetration depth of the irradiation, indicating dissolution of the precipitates. Similar behavior is observed for the other alloy compositions.

3.4. Statistics analysis of the vacancy migration energy barriers

For each of the three Cu–Cr–Ta compositions that were experimentally tested and characterized, NEB calculations were performed to obtain the vacancy MEB with the aim of elucidating the influence of the potential energy landscape (PEL) on void formation propensity in each alloy. To obtain statistically meaningful distributions of vacancy MEBs, no explicit separation by atomic species was applied. Instead, an effective system-wide diffusivity was evaluated by considering the atomic species occupying the twelve nearest-neighbor sites surrounding a central vacancy in randomly generated simulation cells. Consequently, the resulting statistics inherently reflect the compositional abundance of each element and its likelihood of appearing in the local neighboring environment. Figure 8 shows violin plots for the vacancy MEB for each of the copper alloys. The median, mean, and percentile range equivalent to $\pm 1\sigma$ are indicated by solid, dashed, and dash-dotted lines, respectively.

Table 4: Summary of the different properties evaluated on the three systems of Cu alloys.

Technique	Property	Cu- 5at.%Cr- 2.5at.%Ta	Cu- 9at.%Cr- 4at.%Ta	Cu- 24at.%Cr- 5at.%Ta
TGS	f_{SAW} drop [%] (@DPA)	-0.30 (0.07)	-0.54 (0.07)	-1.27 (0.19)
TEM	Void density [#/ μm^2]	710	1065	2715
NEB	$\eta_{MEB}[eV]$	0.658	0.673	0.655
	$\mu_{MEB}[eV]$	0.685	0.678	0.675
	$\sigma_{MEB}[eV]$	0.184	0.197	0.304
	$LB\sigma_{MEB}[eV]$	0.534	0.532	0.397

4. Discussion

4.1. Alloy system selection

CALPHAD predictions of thermal conductivity evolution with temperature on different Cu–Cr–X alloy systems indicate that tantalum is the most

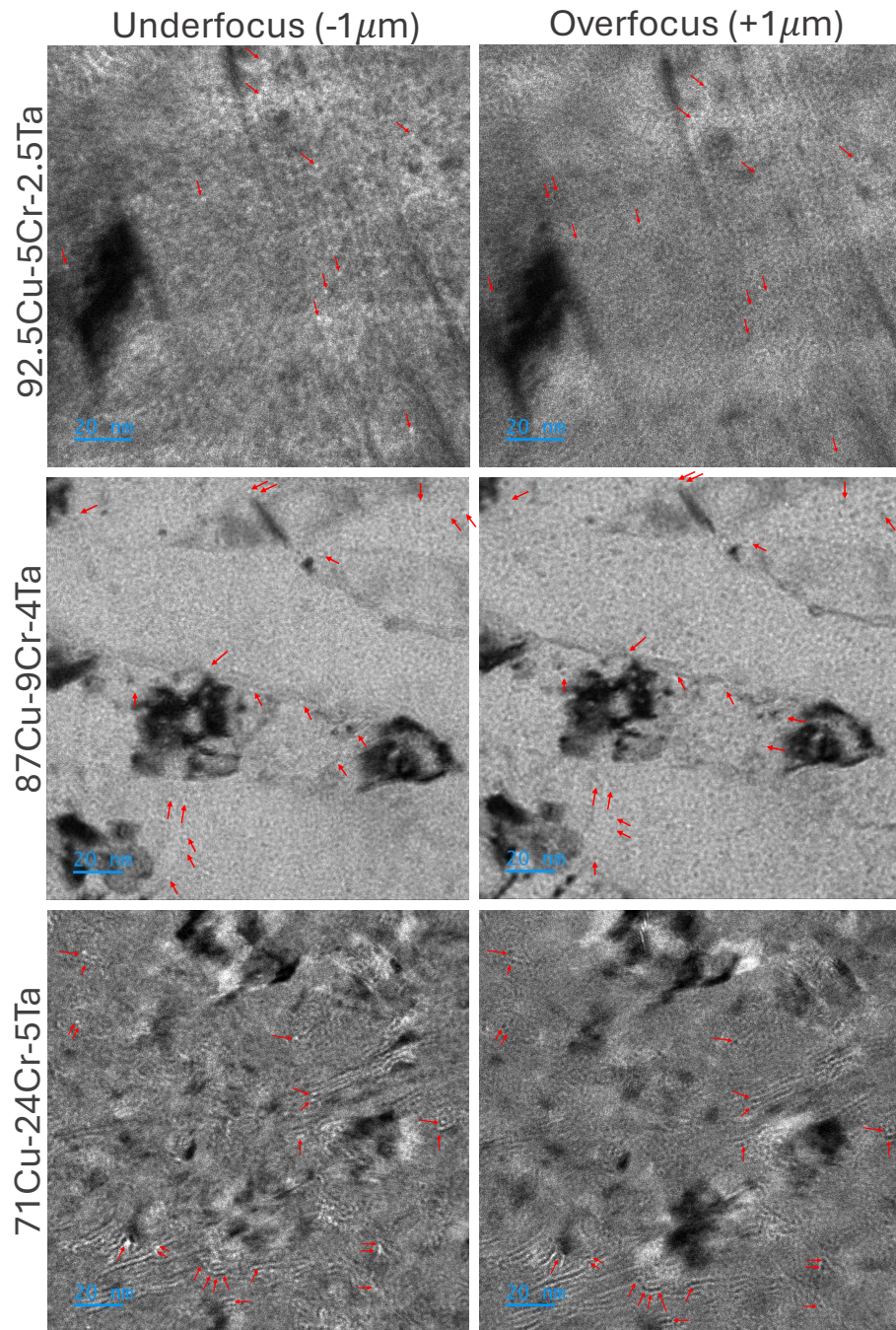


Figure 5: TEM images from the different Cu-Cr-Ta compositions. On the left side pictures were taken with an underfocus value of $-1\mu\text{m}$, and images on the right column were taken with an overfocus value of $+1\mu\text{m}$. Red arrows point out the voids.

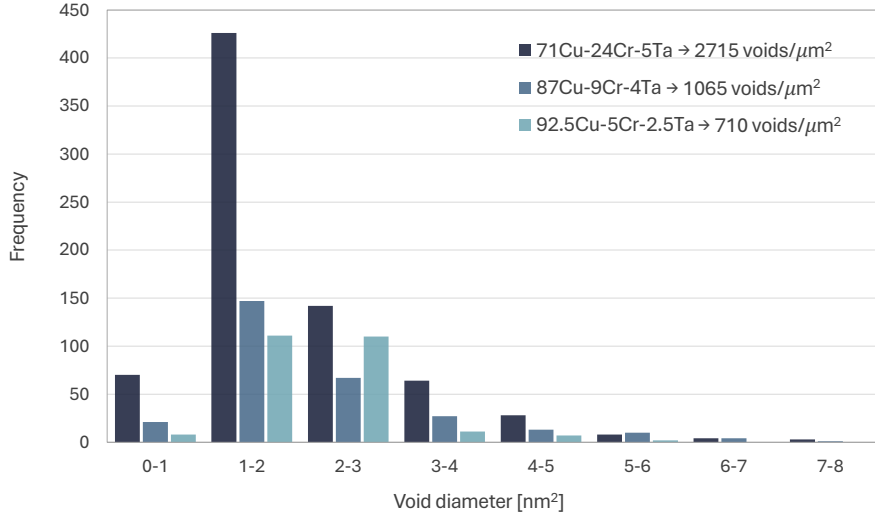


Figure 6: Void number and size distributions for each sample. Void density (voids per μm^2) for each composition is shown in the upper-right corner.

effective alloying element for RF antenna materials. In addition to preserving favorable thermal and electrical transport properties, Ta promotes precipitation strengthening through the formation of C15 Laves phase precipitates dispersed within the copper matrix. These combined characteristics are particularly relevant for applications requiring both high heat removal capability and mechanical stability under service conditions. Beyond thermophysical performance, radiological considerations play a critical role in alloy selection for RF antennas for fusion reactors. The allowable Ta concentration range defined by the Fetter limits (6–8 at.%) [14] provides sufficient compositional flexibility to achieve meaningful precipitate strengthening while maintaining a low activation response under fusion spectrum neutron irradiation. When considered alongside the CALPHAD results, these constraints highlight the Cu–Cr–Ta system as a well-balanced solution, offering a favorable compromise between thermal performance, microstructural stability, and radiological viability. Consequently, Cu–Cr–Ta emerges as a strong candidate system for fusion-relevant components such as RF antennas, diagnostics, and normally-conducting magnet coils which may experience significant neutron irradiation.

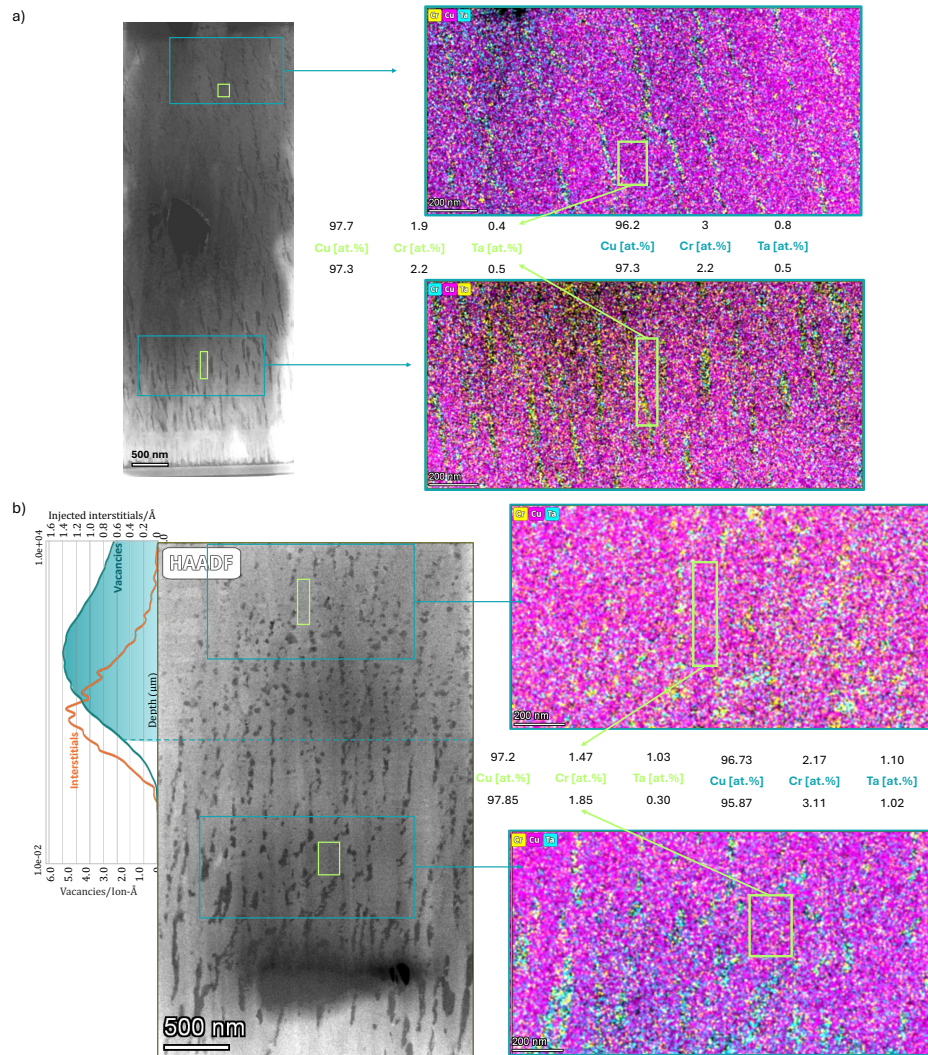


Figure 7: EDS analysis of sample 92.5Cu-5Cr-2.5Ta. a) shows a lamella of the material prior to irradiation and b) shows a lamella of the irradiated material next to the expected damage profile calculated with SRIM, which match the area of the material where no precipitates are found.

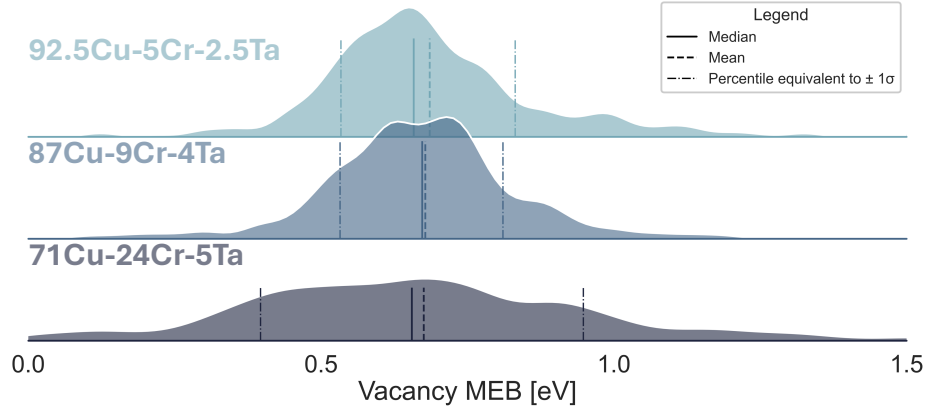


Figure 8: Distribution of the vacancy MEB for the different Cu-Cr-Ta compositions. The solid line denotes the median of the distribution, the dashed line indicates the mean, and the dash-dotted lines corresponds to the equivalent $\pm 1\sigma$ interval.

4.2. Primary radiation damage resistance comparison

As discussed previously, copper-based alloys exhibit saturation of point defects at damage levels of approximately 0.1–0.2 DPA. This behavior is also observed in the three alloys investigated in this study (see Table 4). The evolution of the SAW frequency therefore provides a direct means of tracking changes in material compliance as point defects accumulate during irradiation, considering that vacancies are the main contributor to the thermo-elastic properties of the material, due to their slower diffusivity [37]. Once point defect saturation is reached, additional hardening mechanisms, such as interactions with pre-existing dislocations, between others, become dominant [38], facilitating the identification of this inflection point.

The magnitude of the SAW frequency decrease between the unirradiated state and the saturation point (prior to the subsequent increase in SAW frequency) reflects the extent to which the material softens due to vacancy accumulation. A larger frequency drop indicates a greater increase in compliance, implying a higher retained vacancy population in the microstructure once the equilibrium concentration of point defects has been established. Assuming similar defect evolution mechanisms across the alloys from the compositional space explored, those that generate a larger population of point defects during the primary damage stage are expected to exhibit an increased susceptibility to void formation as irradiation progresses, implying a larger influence on material’s properties.

Conversely, a smaller SAW frequency drop up to the point defect saturation regime indicates reduced vacancy accumulation and, consequently, greater resistance to primary radiation damage. Among the compositions examined here, the Cu-5 at.% Cr-2.5 at.% Ta alloy exhibits the smallest SAW frequency decrease, suggesting superior resistance to primary radiation damage.

This interpretation is further supported by post-irradiation TEM analyses conducted on the I^3TGS samples exposed up to 25 DPA, which reveal trends in void density consistent with those inferred from the SAW frequency decay measurements. Moreover, ratios of void densities between pairs of alloys (e.g., Void density_{92.5Cu-5Cr-2.5Ta} / Void density_{71Cu-24Cr-5Ta}) agree with the corresponding SAW frequency decay ratios to within ± 0.05 . This agreement demonstrates that I^3TGS enables reliable *relative* comparisons of primary radiation damage resistance among alloys fabricated under identical conditions. As such, I^3TGS provides an efficient tool for early-stage compositional down-selection, significantly reducing the need for accelerator time and extensive post-irradiation characterization.

4.3. Radiation-induced void formation explained by vacancy MEB distributions

Several studies have shown that the roughness of the PEL in chemically complex alloys can suppress defect mobility and enhance primary radiation damage resistance. Jin et al. [39] established a link between system mixing energy, heterogeneity in defect MEBs, and radiation tolerance in NiFe solid solutions, demonstrating via molecular dynamics that compositions with larger MEB variance exhibited reduced primary damage. On the other hand, Xu et al. [40] claim that in multi-principal element alloys (MPEAs), the mean value of the MEB of each elemental species has a stronger influence on diffusion behavior than the standard deviation of the barrier distribution. This is because the likelihood of an atom making a jump is determined mainly by its average barrier height, while variations around that mean have a comparatively smaller effect. Interestingly, Bin et al. [41] showed that short-range order (SRO) in MPEAs distorts the PEL, producing asymmetric forward and backward migration barriers that act as trapping sites and suppress long-range diffusion. In parallel, high mixing energy has been associated with a reduced propensity for large defect cluster formation following successive radiation cascades [39], while slow energy dissipation has been

proposed as an additional governing mechanism controlling early-stage defect dynamics [42]. Experimental and simulation work by Granberg et al. [34] further demonstrated that equiatomic alloys exhibit enhanced resistance to irradiation-induced amorphization, attributed to lattice distortion that limits dislocation motion and constrains defect cluster growth. Together, these studies indicate that chemical complexity could enhance radiation tolerance through multiple, interconnected mechanisms, all of which ultimately influence defect mobility, recombination, and clustering.

To interpret the experimental observations in the present work, vacancy migration energy barrier calculations were performed for each irradiated composition, and statistical descriptors of the MEB distributions (Figure 8) are shown in Table 4. No direct correlation was found between either the mean or the standard deviation of the vacancy MEB distributions and the void densities measured by TEM. Additionally, as we considered the nearest 12 neighboring positions of the FCC and calculate the vacancy MEB independently of the element on that position, to account for the compositional abundance of each element and its likelihood of appearing nearby to that random vacancy, non-gaussian distributions of the MEB were obtained. Then, as it is an asymmetrical distribution, the median is a more representative value than the mean, in the same way the percentiles equivalent to the $\pm 1\sigma$ of the population have been calculated. Therefore, the analysis of the lower tail of the vacancy MEB distributions reveals a physically meaningful trend. Alloys exhibiting smaller vacancy MEB values at the -1σ level possess a higher fraction of vacancies capable of escaping the cascade region, as the energy that they have to overcome is lower, thereby reducing vacancy–interstitial recombination during continuous irradiation and increasing the probability of void formation in the long term irradiation. Conversely, compositions with larger -1σ MEB values promote more localized vacancy populations, as the diffusivity of those vacancies will take longer, enhancing recombination with cascade-generated interstitials and suppressing void nucleation. These results suggest that radiation damage resistance is governed by the fraction of highly mobile vacancies that control recombination efficiency and defect survival.

4.4. *Precipitate recoil dissolution*

TEM imaging over the full lamella length, before and after self-ion irradiation, reveals clear dissolution of precipitates within the irradiated region. This behavior is noteworthy, as previous studies on Cu–Cr–Nb and

Cu–Cr–Nb–Zr alloys subjected to heavy-ion and neutron irradiation did not report precipitate dissolution [43, 15]. A key distinction between the present samples and those investigated in earlier work lies in the characteristic precipitate size relative to the matrix grain size. While precipitates in the previously reported alloys are typically much smaller than the matrix, the precipitates in this study have a comparable size respect the matrix grains.

The observed behavior can be rationalized in terms of recoil dissolution, in which the relative size of the precipitates with respect to the surrounding matrix grain size governs their stability under irradiation [44]. When precipitate dimensions approach those of the matrix grains, as in the present microstructure, ballistic mixing promotes radiation-induced dissolution. In contrast, smaller precipitates embedded in coarse-grained matrices are more resistant to recoil-driven dissolution and may instead remain stable or even grow under irradiation. Consequently, although precipitate dissolution is observed in the nanostructured PVD samples studied here, such behavior is not expected for bulk Cu–Cr–Ta alloys subjected to similar irradiation conditions.

5. Conclusion

Considering the current limitations in material availability for RF launchers in fusion reactors, the Cu–Cr–Ta alloy system emerges as a promising candidate due to its ability to form C15 Laves phase precipitates, which provide mechanical stability at elevated temperatures while preserving favorable thermal and electrical conductivity and maintaining acceptable levels of WDR. CALPHAD-based screening further supports the selection of Ta as an optimal alloying element, offering improved thermal conductivity performance relative to established benchmarks such as GRCop-84 while satisfying radiological constraints relevant to fusion environments.

In this work, a novel approach for evaluating primary radiation damage resistance was demonstrated using in situ ion irradiation combined with transient grating spectroscopy (I^3TGS). By monitoring the evolution of the surface acoustic wave (SAW) frequency from the unirradiated state to the point defect saturation regime, relative differences in vacancy accumulation among alloys could be quantified in real time. Post-irradiation transmission electron microscopy of samples exposed up to 25 DPA validated this methodology, revealing a strong correlation between the magnitude of the SAW frequency drop and the resulting void density. This agreement confirms that I^3TGS

enables reliable, rapid comparison of radiation damage resistance between alloys fabricated under identical conditions, significantly reducing the reliance on long irradiation campaigns and extensive post-irradiation characterization during early-stage compositional down-selection. Among the investigated compositions within the Cu–Cr–Ta system, the Cu-rich alloy (Cu–5 at.% Cr–2.5 at.% Ta) exhibited the smallest SAW frequency decrease during irradiation, as well as the lowest void density, indicating superior resistance to radiation. Complementary vacancy migration energy barrier analyses suggest that this enhanced performance is associated with a reduced population of highly mobile vacancies, promoting vacancy–interstitial recombination and decreasing void formation.

Data availability statement

The data and code that support the findings of this study are openly available in the following repository: <https://github.com/shortlab/2026-ebotica-CuCrTa-RDRA>.

Declaration of generative AI and AI-assisted technologies in the manuscript preparation process

During the initial preparation of this work, ChatGPT-5 model were used by the main author for English correction and expression. After using this tool, all authors reviewed and edited the content as needed, and take full responsibility for the content of the publication.

CRedit authorship contribution statement

Elena Botica-Artalejo Conceptualization, Methodology, Formal Analysis, Investigation, Writing – Original Draft, Writing – Review & Editing, Visualization. **Gregory M. Wallace** Conceptualization, Methodology, Supervision, Funding acquisition, Writing - Review & Editing. **Michael P. Short** Conceptualization, Methodology, Supervision, Writing - Review & Editing.

Declaration of Competing Interest

The authors declare that they have no known competing financial interests or personal relationships that could have appeared to influence the work reported in this paper.

Funding sources

This work was supported by the U.S. Department of Energy, Office of Science, Office of Fusion Energy Sciences under Award Number DE-SC0024307.

Acknowledgment

This work was performed in part in the MIT.nano Characterization Facilities and in the Center of Nanoscale Systems at Harvard University. Thanks to Aubrey Penn at MIT.nano for her help with the Themis Z G3 Cs-Corrected S/TEM.

References

- [1] G. M. Wallace, T. Bohm, and C. E. Kessel. “Multiphysics Simulations of a Steady-State Lower Hybrid Current Drive Antenna for the FSNF”. In: *Fusion Science and Technology* 77.2 (2021). Publisher: Bellwether Publishing, Ltd., pp. 159–171. ISSN: 19437641. DOI: 10.1080/15361055.2020.1858672.
- [2] Gregory M. Wallace et al. “Ultra-Rapid, Physics-Based Development Pathway for Reactor-Relevant RF Antenna Materials”. en. In: *IEEE Transactions on Plasma Science* (2022), pp. 1–4. ISSN: 0093-3813, 1939-9375. DOI: 10.1109/TPS.2022.3171497.
- [3] S.J. Wukitch, A.H. Seltzman, and J. Ridzon. “DIII-D high field side lower hybrid current drive launcher manufacturing and assembly overview”. en. In: Annapolis, USA, 2023, p. 100001. DOI: 10.1063/5.0163215.
- [4] E Leppink et al. “High-field side scrape-off layer density profile measurements and implications for high-field side LHCD coupling in DIII-D”. en. In: *Plasma Physics and Controlled Fusion* 67.7 (June 2025). Publisher: IOP Publishing, p. 075015. ISSN: 0741-3335. DOI: 10.1088/1361-6587/ade6a8.
- [5] David L Ellis. *GRCop-84: A High-Temperature Copper Alloy for High-Heat-Flux Applications*. English. Tech. rep. NASA TM—2005-213566. ISBN: 3016210134. Cleveland, Ohio: NASA Glenn Research Center, Feb. 2005, p. 29.

- [6] Robert Minneci. “Microstructural Characterization and Analysis of Laser-Powder Bed Fusion GRCop-84 by Metallurgical and Neutron Scattering Methods”. en. PhD thesis. Knoxville: University of Tennessee, May 2021.
- [7] David L Ellis and Dennis J. Keller. *Thermophysical Properties of GRCop-84*. English. Tech. rep. NASA CR-2000-210055. Read pg.4- 5. Cleveland, Ohio: NASA, June 2000, p. 23.
- [8] Pin Yang et al. *Thermal characterization and properties of a copper-diamond composite*. en. Tech. rep. SAND2014-17329, 1322267, 537089. Sept. 2014, SAND2014-17329, 1322267, 537089. DOI: 10.2172/1322267.
- [9] M C I Siu, W L Carroll, and T W Watson. *Thermal conductivity and electrical resistivity of six copper-base alloys*. en. Tech. rep. NBS IR 76-1003. Edition: 0. Gaithersburg, MD: National Bureau of Standards, 1976, NBS IR 76-1003. DOI: 10.6028/NBS.IR.76-1003.
- [10] A. Seltzman and S.J. Wukitch. “Surface roughness and finishing techniques in selective laser melted GRCop-84 copper for an additive manufactured lower hybrid current drive launcher”. In: *Fusion Engineering and Design* 160 (Nov. 2020), p. 111801. DOI: 10.1016/j.fusengdes.2020.111801.
- [11] A. H. Seltzman and S. J. Wukitch. “RF losses in selective laser melted GRCop-84 copper waveguide for an additively manufactured lower hybrid current drive launcher”. In: *Fusion Engineering and Design* 159 (Oct. 2020). Publisher: Elsevier Ltd. ISSN: 09203796. DOI: 10.1016/j.fusengdes.2020.111762.
- [12] Seth A. Hoedl. “Achieving a social license for fusion energy”. en. In: *Physics of Plasmas* 29.9 (Sept. 2022), p. 092506. ISSN: 1070-664X, 1089-7674. DOI: 10.1063/5.0091054.
- [13] R. L. Klueh et al. “Impurity effects on reduced-activation ferritic steels developed for fusion applications”. en. In: *Journal of Nuclear Materials* 280 (2000), pp. 353–359. DOI: 10.1016/S0022-3115(00)00060-X.
- [14] Steve Fetter, E.T Cheng, and F.M Mann. “Long-term radioactive waste from fusion reactors: Part II”. en. In: *Fusion Engineering and Design* 13.2 (Nov. 1990), pp. 239–246. ISSN: 09203796. DOI: 10.1016/0920-3796(90)90104-E.

- [15] Alice Perrin et al. “Microstructure, electrical resistivity, and tensile properties of neutron-irradiated Cu–Cr–Nb–Zr”. en. In: *Frontiers in Nuclear Engineering* 3 (Nov. 2024), p. 1486694. ISSN: 2813-3412. DOI: 10.3389/fnuen.2024.1486694.
- [16] S.J. Zinkle. “Evaluation of high strength, high conductivity CuNiBe alloys for fusion energy applications”. en. In: *Journal of Nuclear Materials* 449.1-3 (June 2014), pp. 277–289. ISSN: 00223115. DOI: 10.1016/j.jnucmat.2013.09.007.
- [17] N. Simos et al. “200 MeV proton irradiation of the oxide-dispersion-strengthened copper alloy (GlidCop-Al15)”. In: *Journal of Nuclear Materials* 516 (Apr. 2019), pp. 360–372. ISSN: 0022-3115. DOI: 10.1016/j.jnucmat.2019.01.026.
- [18] K. S. Kumar et al. “Structural stability of the Laves phase Cr₂Ta in a two-phase Cr–Cr₂Ta alloy”. en. In: *Acta Materialia* 48.4 (Feb. 2000), pp. 911–923. ISSN: 1359-6454. DOI: 10.1016/S1359-6454(99)00377-8.
- [19] Ningyu Li et al. “Achieving Synchronous Improvement in Mechanical Properties and Softening Resistance of Cu-Cr Alloys by Introducing Ta”. en. In: *Journal of Materials Engineering and Performance* 34.17 (Sept. 2025), pp. 19020–19029. ISSN: 1059-9495, 1544-1024. DOI: 10.1007/s11665-024-10575-7.
- [20] Felix Hofmann, Michael P. Short, and Cody A. Dennett. “Transient grating spectroscopy: An ultrarapid, nondestructive materials evaluation technique”. In: *MRS Bulletin* 44.5 (May 2019). Publisher: Cambridge University Press, pp. 392–402. ISSN: 08837694. DOI: 10.1557/mrs.2019.104.
- [21] Angus P. C. Wylie et al. “Accelerating plasma and radiation surface science using transient grating spectroscopy”. en. In: *Review of Scientific Instruments* 96.2 (Feb. 2025), p. 023002. ISSN: 0034-6748, 1089-7623. DOI: 10.1063/5.0232451.
- [22] D. Royer and E. Dieulesaint. “Rayleigh wave velocity and displacement in orthorhombic, tetragonal, hexagonal, and cubic crystals”. en. In: *The Journal of the Acoustical Society of America* 76.5 (Nov. 1984), pp. 1438–1444. ISSN: 0001-4966, 1520-8524. DOI: 10.1121/1.391427.

- [23] Cody A. Dennett and Michael P. Short. “Thermal diffusivity determination using heterodyne phase insensitive transient grating spectroscopy”. In: *Journal of Applied Physics* 123.21 (June 2018). Publisher: AIP Publishing LLCAIP Publishing, p. 215109. ISSN: 0021-8979. DOI: 10.1063/1.5026429.
- [24] O. W. Käding et al. “Transient thermal gratings at surfaces for thermal characterization of bulk materials and thin films”. en. In: *Applied Physics A* 61.3 (Sept. 1995), pp. 253–261. ISSN: 1432-0630. DOI: 10.1007/BF01538190.
- [25] Short Lab. *Github Repository for TGS Postprocessing Scripts*. 2025. DOI: 10.5281/zenodo.2783302.
- [26] James F. Ziegler, M.D. Ziegler, and J.P. Biersack. “SRIM – The stopping and range of ions in matter (2010)”. en. In: *Nuclear Instruments and Methods in Physics Research Section B: Beam Interactions with Materials and Atoms* 268.11-12 (June 2010), pp. 1818–1823. ISSN: 0168583X. DOI: 10.1016/j.nimb.2010.02.091.
- [27] R. E. Stoller et al. “On the use of SRIM for computing radiation damage exposure”. In: *Nuclear Instruments and Methods in Physics Research Section B: Beam Interactions with Materials and Atoms* 310 (Sept. 2013), pp. 75–80. ISSN: 0168-583X. DOI: 10.1016/j.nimb.2013.05.008.
- [28] ASTM. *ASTM E521-23 Standard Practice for Investigating the Effects of Neutron Radiation Damage Using Charged-Particle Irradiation*. English. Tech. rep. Designation: E521 - 23. ASTM International, June 2023, p. 22.
- [29] Aakash Yadav et al. “An analytic study of the Wiedemann–Franz law and the thermoelectric figure of merit”. en. In: *Journal of Physics Communications* 3.10 (Oct. 2019), p. 105001. ISSN: 2399-6528. DOI: 10.1088/2399-6528/ab444a.
- [30] Elena Botica-Artalejo, Gregory Wallace, and Michael P. Short. *Real-time vacancy concentration evolution revealed via heavy ion irradiation experiments*. arXiv:2602.18608 [cond-mat]. Feb. 2026. DOI: 10.48550/arXiv.2602.18608.

- [31] S. J. Zinkle and K. Farrell. “Void swelling and defect cluster formation in reactor-irradiated copper”. In: *Journal of Nuclear Materials* 168.3 (Dec. 1989), pp. 262–267. ISSN: 0022-3115. DOI: 10.1016/0022-3115(89)90591-6.
- [32] S.A. Fabritsiev et al. “The effect of neutron spectrum on the mechanical and physical properties of pure copper and copper alloys”. In: *Journal of Nuclear Materials* 233-237 (Oct. 1996), pp. 526–533. DOI: 10.1016/S0022-3115(96)00260-7.
- [33] B N Singh and S.J. Zinkle. “Defect accumulation in pure fcc metals in the transient regime: a review”. In: *Journal of Nuclear Materials* 206 (1993), pp. 212–229.
- [34] F. Granberg et al. “Mechanism of Radiation Damage Reduction in Equiatomic Multicomponent Single Phase Alloys”. eng. In: *Physical Review Letters* 116.13 (Apr. 2016), p. 135504. ISSN: 1079-7114. DOI: 10.1103/PhysRevLett.116.135504.
- [35] Emmanouil Trachanas et al. “Study of thermal diffusivity degradation on Cu-OFE copper due to proton and self-ion irradiation using in situ transient grating spectroscopy”. en. In: *Journal of Nuclear Materials* 607 (Mar. 2025), p. 155674. ISSN: 00223115. DOI: 10.1016/j.jnucmat.2025.155674.
- [36] David B. Williams and C. Barry Carter. *Transmission electron microscopy: a textbook for materials science*. en. 2nd ed. Vol. 1. Read pg. 96, 163. New York: Springer, 2008. ISBN: 978-0-387-76500-6.
- [37] A. B. Sivak, D. N. Demidov, and P. A. Sivak. “Diffusion Characteristics of Self-Point Defects in Copper: Molecular Dynamic Study”. en. In: *Physics of Atomic Nuclei* 85.7 (Dec. 2022), pp. 1245–1255. ISSN: 1063-7788, 1562-692X. DOI: 10.1134/S1063778822070171.
- [38] Cody A. Dennett et al. “The dynamic evolution of swelling in nickel concentrated solid solution alloys through in situ property monitoring”. en. In: *Applied Materials Today* 25 (Dec. 2021). arXiv:2104.14576 [cond-mat], p. 101187. ISSN: 23529407. DOI: 10.1016/j.apmt.2021.101187.

- [39] Miaomiao Jin, Penghui Cao, and Michael P. Short. “Thermodynamic mixing energy and heterogeneous diffusion uncover the mechanisms of radiation damage reduction in single-phase Ni-Fe alloys”. In: *Acta Materialia* 147 (Apr. 2018). Publisher: Pergamon, pp. 16–23. ISSN: 1359-6454. DOI: 10.1016/J.ACTAMAT.2017.12.064.
- [40] Biao Xu et al. “Mechanism of sluggish diffusion under rough energy landscape”. en. In: *Cell Reports Physical Science* 4.4 (Apr. 2023), p. 101337. ISSN: 26663864. DOI: 10.1016/j.xcrp.2023.101337.
- [41] Xing Bin et al. “Short-range order localizing diffusion in multi-principal element alloys”. In: *Scripta Materialia*. 114450th ser. 210 (Mar. 2022). ISSN: 1359-6462. DOI: 10.1016/j.scriptamat.2021.114450.
- [42] Yanwen Zhang et al. “Influence of chemical disorder on energy dissipation and defect evolution in concentrated solid solution alloys”. In: *Nature Communications* 6 (Oct. 2015), p. 8736. ISSN: 2041-1723. DOI: 10.1038/ncomms9736.
- [43] A.H. Seltzman and S.J. Wukitch. “Nuclear response of additive manufactured GRCop-84 copper for use in Lower hybrid launchers in a fusion environment”. en. In: *Fusion Engineering and Design* 159 (Oct. 2020), p. 111726. ISSN: 09203796. DOI: 10.1016/j.fusengdes.2020.111726.
- [44] Gary S. Was. *Fundamentals of Radiation Materials Science*. en. New York, NY: Springer New York, 2017. ISBN: 978-1-4939-3436-2 978-1-4939-3438-6. DOI: 10.1007/978-1-4939-3438-6.Readchapter5..